Research Article

ADVANCED PHOTONICS NEXUS

Generation and control of extreme ultraviolet free-space optical skyrmions with high harmonic generation

Yiqi Fang[a] **and Yunquan Liu**[a,b,c,*]

[a]Peking University, School of Physics, State Key Laboratory for Mesoscopic Physics and Frontiers Science Center for Nano-Optoelectronics, Beijing, China

[b]Shanxi University, Collaborative Innovation Center of Extreme Optics, Taiyuan, China

[c]Beijing Academy of Quantum Information Sciences, Beijing, China

Abstract. Optical skyrmion serves as a crucial interface between optics and topology. Recently, it has attracted great interest in linear optics. Here, we theoretically introduce a framework for the all-optical generation and control of free-space optical skyrmions in extreme ultraviolet regions via high harmonic generation (HHG). We show that by employing full Poincaré beams, the created extreme ultraviolet fields manifest as skyrmionic structures in Stokes vector fields, whose skyrmion number is relevant to harmonic orders. We reveal that the generation of the skyrmionics structure is attributed to spatial-resolved spin constraint of HHG. Through qualifying the geometrical parameters of full Poincaré beams, the topological texture of extreme ultraviolet fields can be completely manipulated, generating the Bloch-type, Néel-type, anti-type, and higher-order skyrmions. We promote the investigation of topological optics in optical highly nonlinear processes, with potential applications toward ultrafast spintronics with structured light fields.

Keywords: skyrmions; Poincaré beam; high harmonic generation; spin-orbit interaction.

Received May 31, 2023; revised manuscript received Jul. 16, 2023; accepted for publication Aug. 1, 2023; published online Aug. 14, 2023.

© The Authors. Published by SPIE and CLP under a Creative Commons Attribution 4.0 International License. Distribution or reproduction of this work in whole or in part requires full attribution of the original publication, including its DOI.

[DOI: 10.1117/1.APN.2.4.046009]

1 Introduction

Skyrmions[1] are topological defects in vector fields, which can be created, moved, and annihilated. They are ubiquitous and important in condensed matter physics.[2,3] Recently, the idea of skyrmions was introduced into the communities of photonics and optics.[4] The optical analogies of skyrmions have found advanced applications in various fields such as topological Hall devices[5] and deep-subwavelength microscopy.[6] An optical skyrmion can be realized when the values of electromagnetic vector fields[4,6–8] or Stokes vector fields[9–11] are taken to fully cover a unit sphere (4π) within the skyrmionic boundaries. It was first discovered that one can generate optical skyrmions in the form of surface plasmon polaritons by interacting light with nanostructures.[4] Later, the generation of free-space optical skyrmions was proposed and realized through spatial light modulation methods with digital holography[10,12] and optical focusing.[13] All these methodologies concentrate on linear optical processes. Owing to the rigid requirement of the local state of polarization for skyrmionic vector textures, the manifestation and manipulation of short-wavelength optical skyrmions are extremely rare.

High harmonic generation (HHG) is a typical highly nonlinear process in ultrafast science,[14] through which the fundamental driving photons can be up-converted to a wide spectral region from vacuum ultraviolet to the X-ray domain.[15] In HHG, the local states of driving laser fields are inherently resolved with sub-nanoscale spatial resolution of light–atom interaction. This nature promotes the emerging HHG studies to produce novel spatially structured light beams,[16–23] which has shown great potential in sculpting extreme-ultraviolet (EUV) and soft X-ray lights. Optical skyrmions in visible light have demonstrated relevant applications in displacement sensing.[24] Looking forward, the creation of EUV optical skyrmions will offer appealing opportunities for ultra-fast and -micro metrology, since they

*Address all correspondence to Yunquan Liu, yunquan.liu@pku.edu.cn

can provide totally opposite spin states in small spatial scales, allowing a high degree of controllability when they participate directly in optical nonlinear interaction. It is highly demanding to use HHG to shape EUV fields with a polarization-dependent topological structure in a controlled manner. However, due to the electron recollision nature, the polarization control of HHG is not straightforward. The intersection between HHG and optical skyrmions has therefore remained untapped, which impedes further exploration of topological light in the EUV region.

In this work, we show how to create and control EUV free-space optical skyrmions. By employing HHG as the highly nonlinear interaction process and full Poincaré beams with different wavelengths as the driving fields, we demonstrate that the generated EUV fields reveal explicit skyrmionic structures in Stokes vectors. Their skyrmion numbers are determined by monitoring the polarity and vorticity of Stokes vector distributions, which manifest a close correction with the harmonic orders. We reveal that the underlying mechanism is related to spatial-resolved spin constrain in HHG. More importantly, we further propose, by employing the concept of hybrid-order Poincaré sphere pairs (HyOPSP), a novel control scenario for the topological texture of the EUV skyrmions. In this way, we show that with controlling the geometrical parameters of the driving full Poincaré beams, one can form arbitrary crucial EUV skyrmionic textures (e.g., Bloch-type, Néel-type, anti-type, and higher-order skyrmions) in HHG. This controlling strategy can be extended to other nonlinear optical processes.

2 Results

2.1 Signatures of the Driving Structured Fields

The full Poincaré beam is a typical vector field, whose polarization state covers the full surface of the Poincaré sphere. It is constructed by an arbitrary-order Laguerre–Gaussian beam and a fundamental Gaussian mode with an orthogonal polarization state. Its electric field can be given by: $\mathbf{E}_{i,\omega}(\mathbf{r}_i,t) = e^{-i\omega t}[u_\omega e^{i\ell\omega\varphi i}(\mathbf{e}_x + i\mathbf{e}_y) + u'_\omega e^{i\ell'\omega\varphi i}(\mathbf{e}_x - i\mathbf{e}_y)] + c.c.$, where t is the time, ω is the angular frequency, $\mathbf{r}_i = (\rho_i, \varphi_i)$ denotes the spatial coordinate for the incident driving fields [the notation "i" indicates the variables in the incident plane, as shown in the inset of Fig. 1(a)], u_ω (u'_ω) is the spatial complex amplitude, and ℓ_ω (ℓ'_ω) is the topological charge (ℓ_ω or ℓ'_ω equals zero). Without loss of generality, u_ω (u'_ω) can be approximated as a complex constant for the incident laser. For conciseness, we introduce a geometrical parameter defined as $\eta_\omega = (\ell_\omega, \ell'_\omega, |u'_\omega|/|u_\omega|, \arg(u'_\omega) - \arg(u_\omega))$. As shown later, η_ω directly determines the topology of EUV fields.

To demonstrate our scheme, we start by considering one typical kind of full Poincaré beams, namely, cylindrical vortex vector beams (CVVBs). We illustrate the physical scenario in Fig. 1(a), where the incident field is spatiotemporally superposed by two CVVBs with different wavelengths (800 nm + 400 nm). The geometrical parameters of the 800- and 400-nm CVVBs are given by $\eta_{\omega 1} = (-2,0,1,0)$ and $\eta_{\omega 2} = (0,2,1,0)$. The notations ω_1 and ω_2 represent the angular frequencies of 800 and 400 nm, respectively. As shown in Fig. 1(a), for each CVVB, it carries both radial polarization state (i.e., optical polarization singularity) and spiral phase (optical phase singularity).

In HHG, atoms directly interact with the focal field of the incident laser. It is important to know the signatures of focal field distribution. We, therefore, simulate the focal field of CVVB using the Richards–Wolf vectorial diffraction method.[25] We use the 20th order Gauss–Legendre integral formula to numerically calculate the integral, and the grid size is chosen as 50 μm in the focal plane with a spacing of 0.05 μm. In our simulation, the numerical aperture (NA) is selected to be NA = 0.02. It is a typical focusing condition of HHG experiments. In this way, we can obtain the focal intensity distributions of both 800- and 400-nm fields [upper panel in Fig. 1(b)]. One can notice that the focal intensity distributions manifest as Gaussian-like structures, which differ from the typical donut-shaped structure of individual phase or polarization singularity. Such exotic distribution largely enriches the highly nonlinear interaction in the spatial domain. Furthermore, we calculate the normalized spin angular momentum (SAM) density of focal fields.[26,27] As shown in the bottom panel of Fig. 1(b), spatial-varying polarization is generated. It is interesting to find the presence of circular polarizations in the focal plane despite the incident light being linearly polarized throughout. Here, we emphasize that both the peculiar intensity distribution and SAM distribution of the focal field originate from spin-orbit interaction of light.[28] The underlying origin of such spin-orbit interaction comes from the time-varying polarization distribution in the wavefront of incident CVVB.[28,29] When the 800- and 400-nm CVVBs are spatiotemporally synthesized at focus, three-leaf polarizations show up [Fig. 1(c)]. This polarization has played an important role in the studies of HHG, which allows us to emit circularly polarized EUV light in HHG.[30] Most of the relevant works only involve laser fields with a spatially homogeneous three-leaf polarization. In our case, this two-color synthesized field, known as a Lissajous beam,[31,32] carries a versatile polarization state, and the polarization varies rapidly in space.

2.2 Generation of EUV Skyrmions with CVVBs

To explore the HHG driven by the synthesized fields, we perform numerical simulation by solving the Schrödinger equation for hydrogen within strong-field approximation.[33] The high harmonic field with angular frequency ω is calculated from the Fourier components of the dipole moment, $\mathbf{P}(\mathbf{r},\omega) = \omega^2 \int \mathbf{D}(\mathbf{r},t)e^{-i\omega t}\mathrm{d}t$. Here, the dipole moment depends on both space ($\mathbf{r}$) and time (t), given by $\mathbf{D}(\mathbf{r},t) = -i\int_{-\infty}^{t}\mathrm{d}t'[-2\pi i/(t-t'-i\delta)]^{3/2}\mathbf{d}^*[\mathbf{p}_s + \mathbf{A}(\mathbf{r},t)]\cdot\mathbf{E}(\mathbf{r},t')\cdot\mathbf{d}[\mathbf{p}_s + \mathbf{A}(\mathbf{r},t')]\exp[-iS(\mathbf{r},\mathbf{p}_s,t)] + c.c.$, in which δ is an arbitrary small positive constant, $\mathbf{p}_s$ is the saddle point momentum calculated by saddle point equation $\nabla_{\mathbf{p}}S(\mathbf{r},\mathbf{p}_s,t) = 0$, $S(\mathbf{r},\mathbf{p}_s,t) = \int_{t'}^{t}\mathrm{d}t''\{[\mathbf{p} + \mathbf{A}(\mathbf{r},t'')]^2/2 + I_p\}$ is the quasi-classical action, $d^*[.]$ and $d[.]$ contribute to the photoelectron recombination and ionization process, $\mathbf{E}$ is the focal electric field obtained by the Richards–Wolf vectorial diffraction method, and $\mathbf{A}$ is the vector potential of light. We insert the focal electric field into the expression of the HHG dipole moment and obtain the spatially resolved HHG field of different orders by changing the harmonic frequency ω.

In order to elucidate the advantages of the two-color scenario in generating EUV skyrmions, we compare the HHG driven by three different fields, i.e., the 800-nm CVVB, 400-nm CVVB, and their synthesized two-color light field. In simulation, the peak intensities of each driving field are taken to be $I = 5 \times 10^{14}$ W/cm^2, and their temporal envelopes are selected to be a $\sin^2$ function of $\tau = 21.3$-fs duration time. In Figs. 2(a)–2(c), we show the HHG spectra for different drivers. Due to the joint restriction taken by parity, energy, and momentum

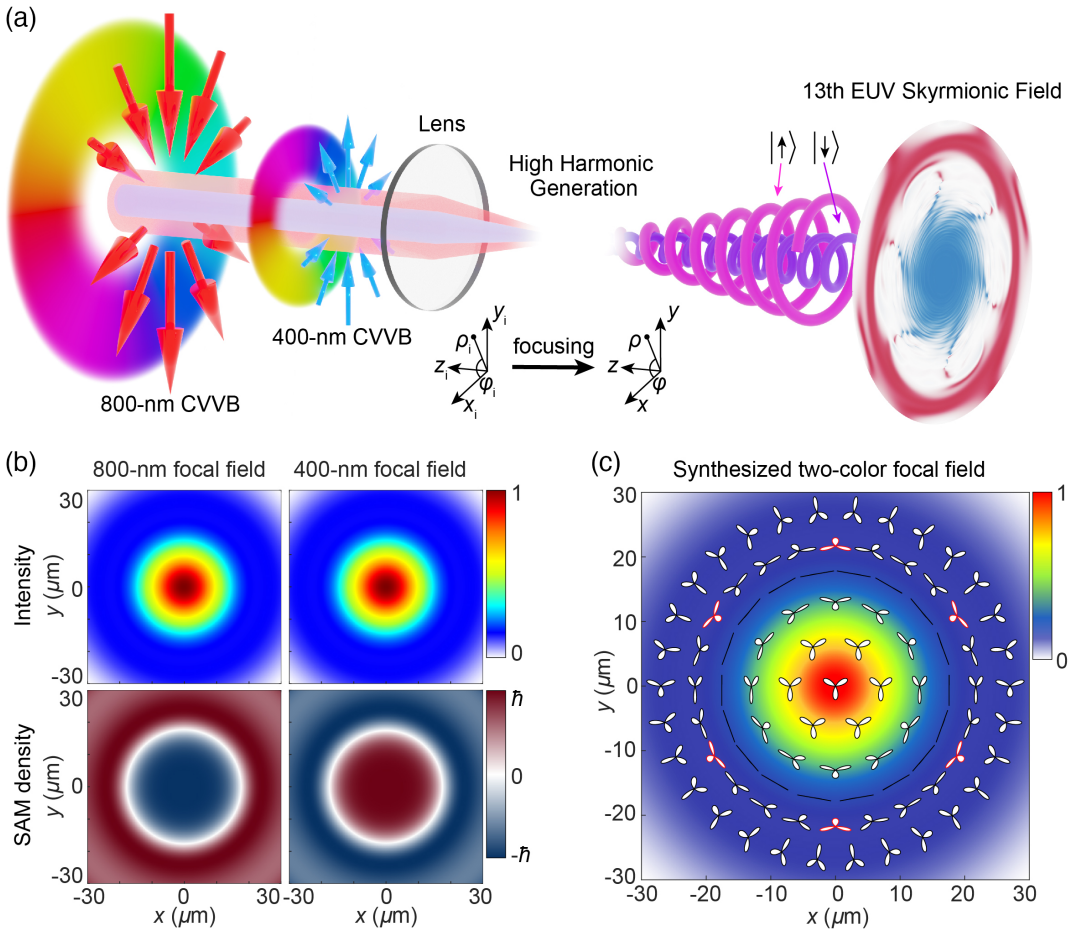

Fig. 1 (a) Schematic of generating EUV skyrmions with HHG. A synthesized two-color (800 nm + 400 nm) CVVB field is employed to generate HHG with non-trivial spatial spin distribution. The red and blue arrows represent the instantaneous electric field vectors of 800- and 400-nm incident fields, respectively, and the accompanied pseudocolor maps show their angular phase structures. We control the beam width of the incident 800-nm field that is twice that of the 400-nm field, so the focal distributions of intensities of 800- and 400-nm CVVBs are the same. We note here that if they are not the same, one cannot generate the skyrmions presented in this work. Here, we show the EUV skyrmionic fields can be generated, and the 13th harmonic spins down at the beam center and spins up at the surrounding. The inset illustrates the coordinates in the incident plane and focal plane, respectively. (b) The distributions of intensity (upper panel) and normalized z-direction SAM density (bottom panel) of 800- and 400-nm CVVBs in the focal plane individually. (c) The focal electric field structure of the two-color synthesized CVVB. The pseudocolor map indicates the intensity distribution of the driving beam. The overlapped Lissajous figures illustrate the local polarization states, in which the red profiles show the sixfold spatial symmetry of the two-color synthesized field.

conservations in HHG, harmonic spectra reveal the orders of $(2n-1)$th, $(4n-2)$th, and nth for the three different drivers, respectively.

In time domain, the generated field in HHG is spatially structured attosecond pulse trains. To identify the real-space topology of the harmonics, we confine one specific frequency of harmonics and extract its spatial intensity distributions [Figs. 2(d)–2(f)]. It can be noticed that when the driver is a single-color CVVB, the harmonics manifest as annulus structures. By contrast, the intensity of harmonics with the two-color driving field is different, which reveals a Gaussian-like structure for $(3n+1)$th and $(3n-1)$th harmonic or annulus structure for $3n$th harmonic. Due to the peculiar polarization texture of the driving two-color beam, the $3n$th harmonic has significantly lower yield than the $(3n \pm 1)$th harmonics. In Figs. 2(g)–2(i), we show the corresponding SAM distributions. For each harmonic, the SAM density is spatially varied. Upon closer inspection, in the case of the two-color CVVB driver, the SAM distribution of produced harmonics reveals a sixfold symmetrical distribution [Fig. 2(i)]. This unique distribution can be attributed to the inherent sixfold symmetry of the driving field, which is illustrated by the red profiles depicted in Fig. 1(c).

To form a skyrmionic field, local SAM should orient oppositely at the center of the field compared to the surrounding. Our simulation indicates that one cannot obtain an explicit EUV skyrmionic field with single-color CVVB drivers in

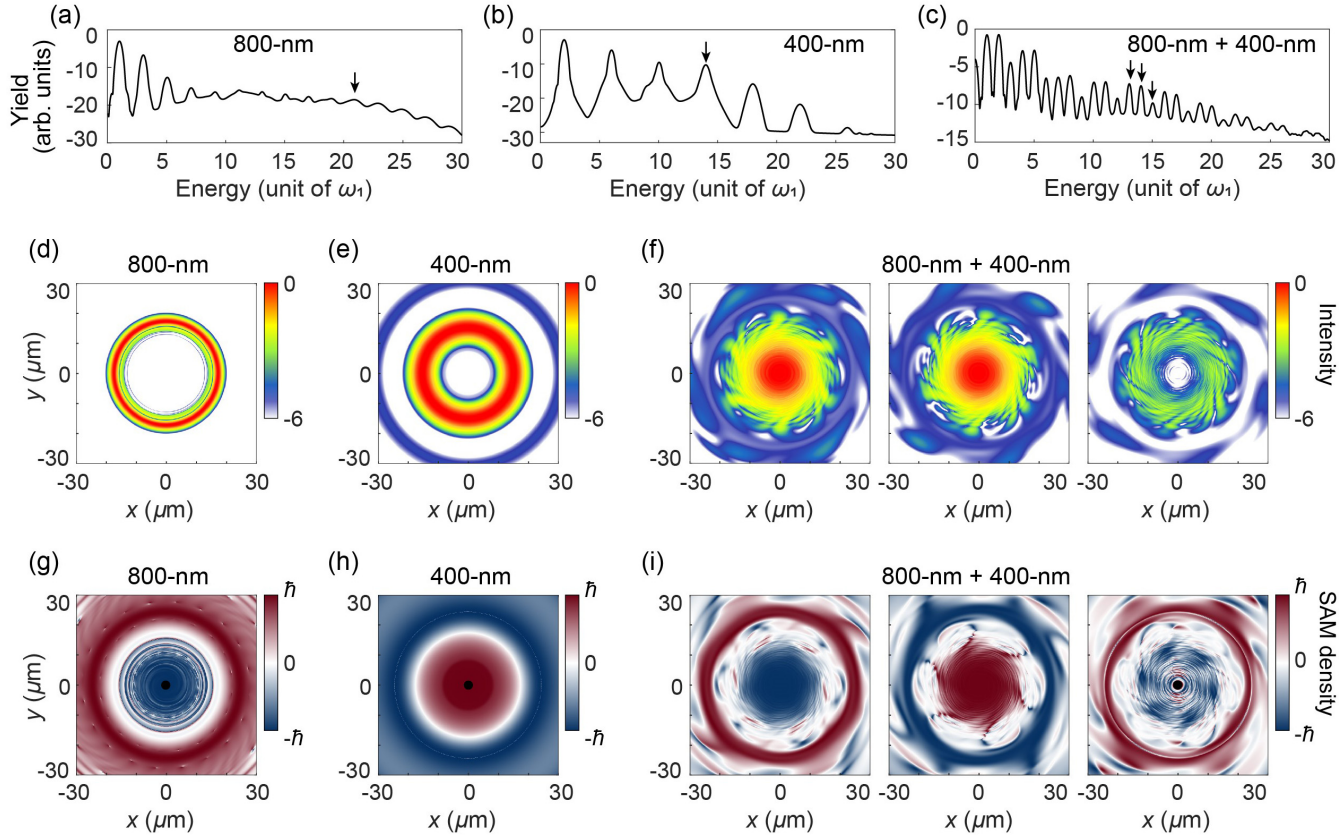

Fig. 2 Spatio–spectral signatures of HHG driven by the CVVBs. (a)–(c) High harmonic spectra. (d)–(f) Spatial intensity distributions of logarithmic scales. (g)–(i) Spatial distributions of normalized SAM densities along the z-direction. The HHG drivers are (a), (d), (g) the 800-nm CVVB, (b), (e), (h) 400-nm CVVB, and (c), (f), (i) their synthesized two-color CVVB. The harmonic orders marked by black arrows in (a)–(c) correspond to each column in (d)–(i).

HHG. This is because the recollision of electrons is rigidly forbidden in a single-color circularly polarized local field,[15] resulting in an extremely low photon yield at the center of the harmonic beam [as shown in Figs. 2(d) and 2(e)]. Consequently, the spatial spin reversal is not complete. By contrast, such obstacles can be overcome in the $(3n \pm 1)$th harmonics with a two-color driver. In this case, the yield at the center is substantial, and the SAM is oriented oppositely at the center compared with the surrounding, leading to a non-trivial real-space topology.

To prove that the created $(3n \pm 1)$th harmonics from two-color CVVB fields are skyrmions, we then analyze their spatial vector texture. Conventionally, skyrmions are characterized by skyrmion number Q, defined as[34] $Q = (1/4\pi) \cdot \iint_{\rho 0} \mathbf{S} \cdot (\partial_x \mathbf{S} \times \partial_y \mathbf{S}) \mathrm{d}x\, \mathrm{d}y$, where $\mathbf{S}(x, y)$ and $\rho \leq \rho_0$ denote the vector fields and the defined region for constructing skyrmions in the (x, y) plane. The vector fields of a two-dimensional skyrmion can be written as $\mathbf{S}[\rho \cos(\varphi), \rho \sin(\varphi)] = \{\cos[\alpha(\varphi)] \sin[\beta(\rho)],\ \sin[\alpha(\varphi)] \sin[\beta(\rho)], \cos[\beta(\rho)]\}$, where ρ and φ are polar coordinates in the focal plane, and α and β are spherical coordinates in the Poincaré sphere, as shown in Fig. 3(a). In this way, Q reads

$$Q = \frac{1}{2}\{\cos \beta(\rho)]_{\rho=0}^{\rho=\rho_0} \cdot \frac{1}{2\pi}[\alpha(\varphi)\}_{\varphi=0}^{\varphi=2\pi} = q \cdot m. \tag{1}$$

The skyrmion number is divided into two integers, q and m, in which q describes the polarity of skyrmions, and m indicates the vorticity of skyrmions, respectively. In order to create a skyrmionic field, q and m should both be non-zero. That is, the field vector has to be reversed, comparing the center $\rho = 0$ with its confinement $\rho = \rho_0$, and, meanwhile, it should also cover the unit Poincaré sphere as ρ increases from $\rho = 0$ to $\rho = \rho_0$.

In our configuration, the focal light field can be approximated as a paraxial beam, and thus we explore the possibility of generating EUV fields with a skyrmionic structure in Stokes vector fields, $\mathbf{S} = (S_1, S_2, S_3)$. Each parameter of $\mathbf{S}$ corresponds to an expectation value of a Pauli matrix for a photonic spin state. The skyrmionic boundary is selected to be $\rho_0 = 24\ \mu$m, in which the focal 800- and 400-nm driving CVVBs are circularly polarized. We then inspect the topological character of the skyrmions by the stereographic projection of Stokes vectors [Figs. 3(b)–3(d)]. One can notice that the Stokes vectors point to the opposite direction at $\rho = 0$ and $\rho = \rho_0$, and their orientations change in a vortex type [Figs. 3(c) and 3(d)]. To obtain the specific topological charge, Q, we inspect the azimuthal and radial variation of the Stokes vector distribution [Fig. 3(b)]. It can be seen that the direction of the Stokes vector is changed from downward (upward) to upward (downward) for the 13th (14th) harmonic. This indicates that the polarities of the 13th

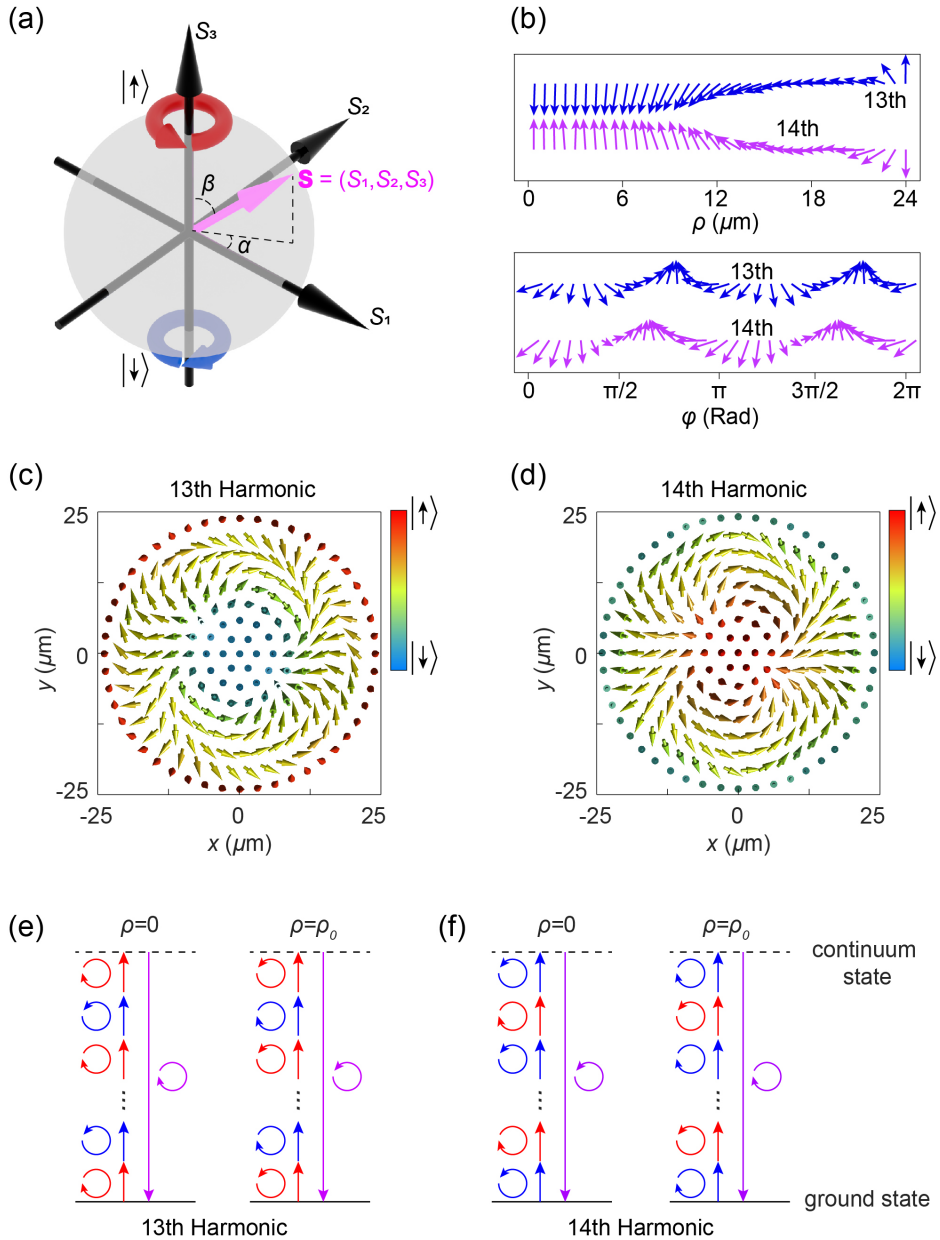

Fig. 3 Characterization of the EUV skyrmions in HHG. (a) Unit Poincaré sphere defined by the normalized Stokes parameters, $\mathbf{S} = (S_1, S_2, S_3)$. At the north and south poles of the Poincaré sphere, polarizations are spin-up and spin-down, respectively. (b) The projection of Stokes parameters of 13th and 14th harmonics in the $S_1 - S_3$ plane as a function of radial distance (upper panel) and the projection in the $S_1 - S_2$ plane as a function of azimuthal angle (lower panel). (c), (d) Spatial distributions of Stokes vectors for the 13th and 14th harmonics in the focal plane, in which the color scheme of the Stokes vector is encoded by the value of S_3. (e), (f) Physical picture of generating skyrmions in HHG.

and 14th harmonics are given by $q_{13} = -1$ and $q_{14} = 1$, respectively. Besides, their transverse components rotate twice counterclockwise from $\varphi = 0$ to $\varphi = 2\pi$, meaning the vorticity of the skyrmion is given by $m_{13} = m_{14} = 2$. Taking both the polarity and vorticity of skyrmions into account, the skyrmion numbers can be determined to be $Q_{13} = q_{13} \cdot m_{13} = -2$ and $Q_{14} = q_{14} \cdot m_{14} = 2$ for these two high harmonics, respectively. Such EUV skyrmionic fields can be categorized as two-order skyrmions.[3]

It is interesting to note that the skyrmion number is dependent on harmonic order. In the picture of absorbing photons, the allowed photon absorption channel for specific harmonics can be written by $(n_{\omega 1}, n_{\omega 2})$, in which $n_{\omega 1}$ and $n_{\omega 2}$ denote the number of photons absorbed from 800- and 400-nm CVVBs. Since the driving field is spatially structured, the allowed photon channel is spatially varied. However, the allowed photon absorption channels cannot be solely determined at the positions in $0 < \rho < \rho_0$, but the channel is well known at $\rho = 0$ and

$\rho = \rho_0$. There, the channel is given by (5, 4) for the 13th harmonic. That is, the number of absorbed 800-nm photons is one more than the number of 400-nm photons. Therefore, the local spin states at $\rho = 0$ and $\rho = \rho_0$ are the same as that of the 800-nm photons for the 13th harmonic [Fig. 3(e)]. Similarly, the corresponding photon channel of the 14th harmonic is (4, 5), and thus the local spin is the same as the 400-nm photon at $\rho = 0$ and $\rho = \rho_0$ [Fig. 3(f)]. As shown in Fig. 1(b), the local spin of 800- and 400-nm CVVBs is inverse, leading to opposite polarities of the 13th and 14th EUV skyrmions. On the other hand, the vorticity of EUV skyrmions is influenced by the focal phase distribution of the 800- and 400-nm CVVBs, which is independent of the harmonic order. Hence, the vorticities are the same for the 13th and 14th skyrmions. As a result, the skyrmion numbers of the 13th and 14th skyrmions are opposite.

2.3 Complete Control Over the Texture of EUV Skyrmions

The behaviors and stabilization of skyrmions highly depend on their topological texture, and thus we then demonstrate how to control the topology of EUV skyrmions. We extend the driving fields from CVVBs to general full Poincaré beams, and we also resort to the synthetization of two-color (800 and 400 nm) beams. To this end, we start by giving an analytical expression for the focal field of full Poincaré beams as

$$\mathbf{E}(\mathbf{r}, t) = e^{-i\omega t} C[u U_\ell e^{i\ell\varphi}(\mathbf{e}_x + i\mathbf{e}_y) + u' U_{\ell'} e^{i\ell'\varphi}(\mathbf{e}_x - i\mathbf{e}_y)] + c.c., \tag{2}$$

where $C = i^\ell kf/2$ (k is the wavenumber, f is the focal distance) and U_ℓ are introduced by optical focusing. U_ℓ modulates the complex amplitude of focal field, and it is expressed as

$$U_\ell = \int_0^{\theta_m} \cos^{\frac{1}{2}}\theta \sin\theta(\cos\theta + 1) J_\ell(\zeta) \mathrm{d}\theta, \tag{3}$$

where J_ℓ stands for the ℓ-order Bessel function of the first kind, and θ is the polar angle in the output pupil whose maximum value, θ_m, is determined by the NA of the lens. Here, it should be noted that for a full Poincaré beam, its topology is largely determined by the phase difference between its two orthogonal components, $\mathbf{e}_x + i\mathbf{e}_y$ and $\mathbf{e}_x - i\mathbf{e}_y$. According to Eq. (3), the sign of U_ℓ endows additional phase difference between these two components beyond the initial one, $\arg(u) - \arg(u')$. It implies that the focusing process itself modulates the topology of the laser field, exerting a significant influence on the topology of EUV skyrmions in HHG.

With Eq. (2), we then propose two empirical restriction rules for the geometrical parameters η of 800- and 400-nm incident full Poincaré beams, which ensure the generated EUV fields in HHG exhibit skyrmionic characteristics. (i) Considering the spin constraints in HHG, the local SAMs of 800- and 400-nm full Poincaré beams should have opposite orientations in the focal plane. It requires that the third components of their Stokes vectors ($S_{3,\omega1}$ and $S_{3,\omega2}$) exhibit opposite signs, leading to

$$\ell_{\omega1} = -\ell'_{\omega2}, \ell'_{\omega1} = -\ell_{\omega2}, \quad \text{and} \quad |u'_{\omega1}|/|u_{\omega1}| = |u_{\omega2}|/|u'_{\omega2}|. \tag{4}$$

(ii) The transverse components of Stokes vectors (i.e., S_1 and S_2) determine the direction of the long-axis of the focal electric field ellipse. To create regular spatial polarization distributions for harmonics, $S_{1,\omega1}$ and $S_{2,\omega1}$ need to be the same as $S_{1,\omega2}$ and $S_{2,\omega2}$, respectively. According to Eq. (2), S_1 and S_2 are determined by the relative phase between right- and left-handed components, i.e., $\arg(uU_\ell) - \arg(u'U_{\ell'})$. Thus, the two-color full Poincaré beams are further confined by

$$\frac{\pi}{2}(\kappa_{\omega1} - \kappa'_{\omega1}) - [\arg(\mu'_{\omega1}) - \arg(\mu_{\omega1})] = \frac{\pi}{2}(\kappa_{\omega2} - \kappa'_{\omega2}) - [\arg(\mu'_{\omega2}) - \arg(\mu_{\omega2})], \tag{5}$$

in which $\kappa = [\mathrm{sign}(\ell)]^{|\ell|}[\mathrm{sign}(\ell) = 1$ for $\ell \geq 0$ and $\mathrm{sign}(\ell) = -1$ for $\ell < 0]$ is related to the additional phase introduced by U_ℓ, and $\arg(u') - \arg(u)$ is related with the initial phase of the incident field.

Confined by the above rules, for each 800-nm full Poincaré beam, there is only one qualified 400-nm full Poincaré beam. Taking an 800-nm full Poincaré beam with $\ell_{\omega1} = -1$ and $\ell'_{\omega1} = 0$ as an example, the topological charges of a qualified 400-nm beam should be $\ell_{\omega2} = 0$ and $\ell'_{\omega2} = 1$. Then, to visualize our controlling strategy of EUV skyrmions, we employ the concept of HyOPSP, which is comprised of two hybrid-order Poincaré spheres[35] at different wavelengths. Each point on the sphere represents one specific full Poincaré beam. In Figs. 4(a) and 4(b), we display the corresponding HyOPSP, in which S_1^h, S_2^h, and S_3^h are the redefined Stokes parameters serving as the sphere's Cartesian coordinates. $\Phi = \tan^{-1}(S_2^h/S_1^h) = \arg(u) - \arg(u')$ and $\Theta = \cos^{-1}(S_3^h)$ are the azimuthal angle and pitching angle, respectively. We colorize some points on these two spheres ($\Phi = 0$, $\Theta \in [0, \pi]$ for 800 nm and $\Phi = \pi$, $\Theta \in [0, \pi]$ for 400 nm). The points in the same colors construct the qualified two-color full Poincaré beams which can generate EUV skyrmions in HHG. For each point on the 800-nm hybrid-order Poincaré sphere, one can find a unique point on the 400-nm sphere that meets the above restriction rules [Eqs. (4) and (5)].

Then, we select some typical points on the HyOPSP to demonstrate control over topological textures of skyrmions. At point A, the geometrical parameters of 800- and 400-nm full Poincaré beams are $\eta_{\omega1} = (-1,0,1,0)$ and $\eta_{\omega2} = (0,1,1,\pi)$, respectively. As shown in Figs. 4(c) and 4(d), the HHG simulations demonstrate that the generated EUV fields manifest as Bloch-type skyrmions, whose skyrmion numbers are $Q = 1$ ($q = 1$, $m = 1$) for the 13th harmonic and $Q = -1$ ($q = -1$, $m = 1$) for the 14th harmonic. Through changing the positions on the HyOPSP, the topological texture can be adjusted. At the points B, the geometrical parameters are given by $\eta_{\omega1} = (-1,0,1,\pi/2)$ and $\eta_{\omega2} = (0,1,1,3\pi/2)$, and the resulted harmonic field is revealed as the Néel-type skyrmions of $Q = -1$ ($q = -1$, $m = 1$) [Fig. 4(e)]. Besides the Bloch-type and Neel-type skyrmions, one can also shape the EUV skyrmions with arbitrary topological textures, such as anti-skyrmion of $Q = 1$ ($q = -1$, $m = -1$) [$\eta_{\omega1} = (1,0,1,0)$ and $\eta_{\omega2} = (0,-1,1,\pi)$] [Fig. 4(g)] and third-order skyrmion of $Q = -3$ ($q = -1$, $m = 3$) [$\eta_{\omega1} = (-3,0,1,0)$ and $\eta_{\omega2} = (0,3,1,\pi)$] [Fig. 4(h)]. One can notice that the topology of EUV skyrmions in HHG is closely related with the geometrical parameters of the incident laser. The first two parameters of η control the polarity and

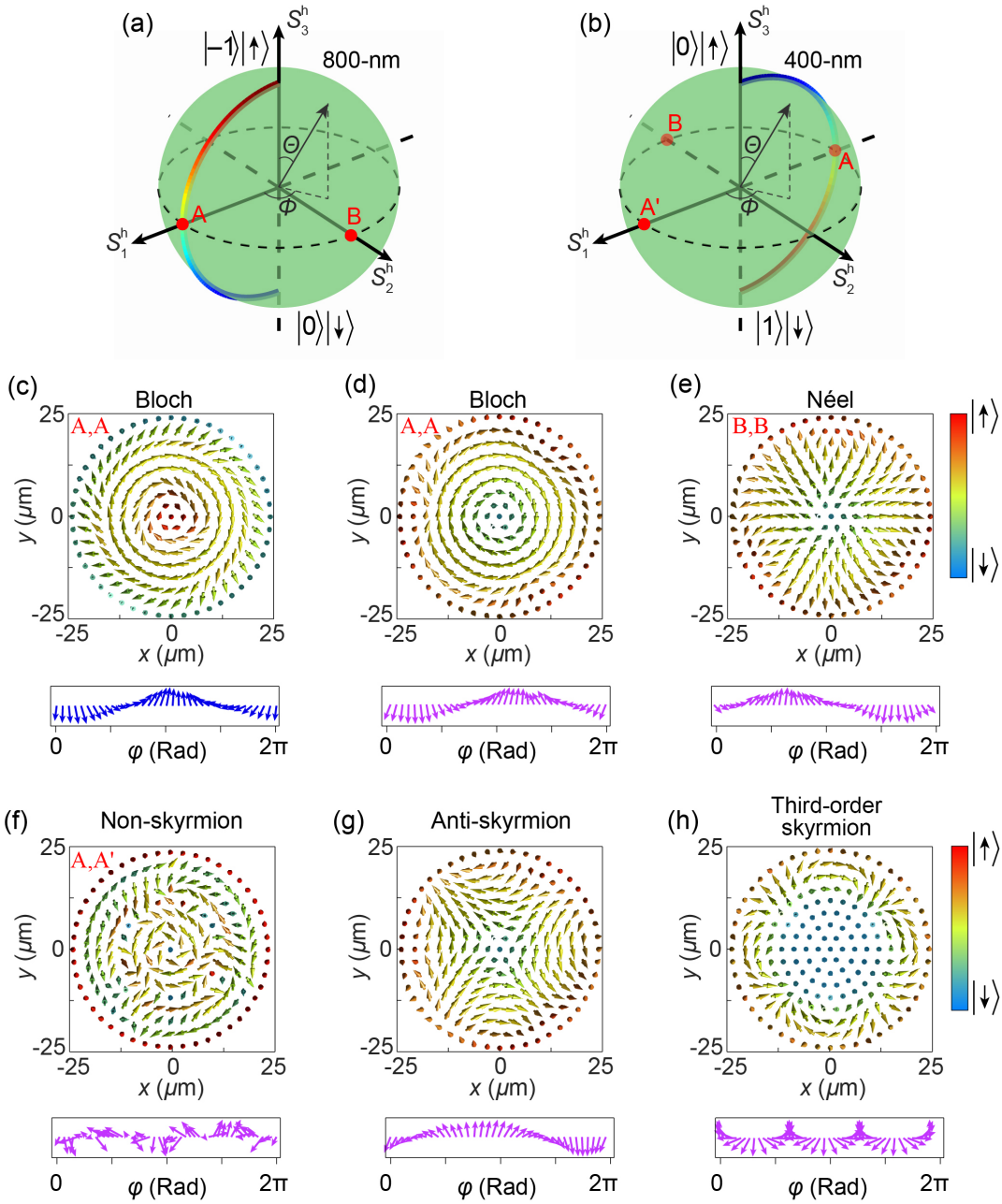

Fig. 4 Control over the topological texture of EUV skyrmions. (a), (b) HyOPSP formed by an 800-nm Poincaré beam ($\ell_{\omega 1} = -1$ and $\ell'_{\omega 1} = 0$) and a 400-nm Poincaré beam ($\ell_{\omega 2} = 0$ and $\ell'_{\omega 2} = 1$). The varying colors on the spheres are used to show the qualified combination of two-color Poincaré beams. Points A and B on the HyOPSP indicate the positions of two-color Poincaré beams, which can generate (c), (d) a Bloch-type EUV skyrmion and (e) a Néel-type EUV skyrmion in HHG. (f) If selecting the point A in the 800-nm sphere and A' in the 400-nm sphere, the generated EUV field reveals a non-skyrmion structure. (g), (h) Formation of anti-skyrmion and third-order skyrmion, respectively. In each diagram, the lower panel shows the projection of Stokes vectors in the S_1-S_2 plane as a function of azimuthal angle. The harmonic orders are 13th for (c) and 14th for (d)–(f).

vorticity of EUV skyrmions, while the last two parameters of η influence the skyrmionic texture (such as Néel-type and Bloch-type).

For comparison, if we select two-color full Poincaré beams that do not satisfy the restriction rules of η, e.g., point A on the 800-nm sphere $[\eta_{\omega 1} = (-1,0,1,0)]$ and point A' on the 400-nm sphere $[\eta_{\omega 2} = (0,1,1,0)]$, one can see that the formed Stokes vectors of the EUV field distribute desultorily, and the HHG field is not a skyrmion [Fig. 4(f)]. Overall, the texture of EUV skyrmions can be controlled using the driving two-color full

Poincaré beams with qualified geometrical parameters. Such a robust methodology shows its uniqueness in free-space optical skyrmions, which has never been unveiled for the optical skyrmions in guided modes or surface plasmon.

3 Discussion and Conclusion

This work demonstrates the generation and control of EUV skyrmions. On the one hand, the generation of EUV skyrmions is rooted in the transfer of photon angular momentum between driving fields and high harmonics. From the view of electron motion, the transfer of photon orbital angular momentum is realized by the spatially resolved recombination time of electrons in the interaction region. As for the transfer of photon SAM, it is first recorded by the ionized electron trajectory (or electron orbital angular momentum) with respect to nucleus and then taken by high harmonics at the instant of recombination. It should be noted that the spin-orbit interaction of light is critical in modifying the distribution of photon angular momentum in the focal plane, giving rise to the generation of EUV skyrmions in HHG. On the other hand, the control of EUV skyrmions is realized by adjusting the spatial mode of two-color driving fields. In principle, the selection of the two-color laser wavelength affects the spectrum of HHG, but it has little influence on the formation and control of EUV skyrmions. Compared with the single-color scenario, the two-color scenario has significant advantages. It introduces more degrees of freedom that allows one to finely control the spatial structure of EUV skyrmionic fields. Moreover, two-color fields enable the creation of bright circularly polarized HHG, where the spin states of driving fields can be imprinted onto different orders of harmonics. Hence, one can sculpt the spatial mode of three-dimensional Stokes parameters for emitted EUV fields [Figs. 4(c)–4(h)]. Here, the employment of HyOPSP presents a clear picture for the configuration of two-color full Poincaré, and it can be easily expanded to many fields, such as four-wave mixing.

To summarize, we have shown theoretically that HHG makes it possible to generate and manipulate the EUV free-space optical skyrmions. The robust control methodology shows its uniqueness in EUV optical skyrmions, which has never been unveiled for optical skyrmions in surface plasmon polaritons or guided modes. This work presents an important interface between strong-field physics and topology.[36,37] The generation and control of EUV skyrmions open a door to access skyrmionic dynamics in the broad ultraviolet region. Magnetic skyrmion Hall effect has been experimentally discovered recently;[38] however, to our knowledge, its optical analog has only been studied in theory.[6] Since the EUV optical skyrmions reveals a regular spatial distribution of the photon spin-orbital state, its highly nonlinear process and ability in ultrahigh spatial resolution may enable the observation of the optical skyrmion Hall effect. Looking broadly, the EUV skyrmions endow one laser beam with totally opposite chiral responses when interacting with chiral matters, and, thus, it could offer new opportunities in the studies of laser-based spatial separation of enantiomers via photoionization. Furthermore, due to the elaborate spatial polarization structure of the EUV skyrmion, it also has implications in HHG-induced EUV nanoscale imaging.[39]

Code, Data, and Materials Availability

Data underlying the results presented in this paper may be obtained from the authors upon reasonable request.

Acknowledgments

We thank the National Key R&D Program (Grant No. 2022YFA1604301) and National Science Foundation of China (Grant Nos. 92050201 and 92250306) for the financial support. The authors declare no conflicts of interest.

References

1. T. H. R. Skyrme, "A unified field theory of mesons and baryons," *Nucl. Phys.* **31**, 556–569 (1962).
2. Y. Tokura and N. Kanazawa, "Magnetic skyrmion materials," *Chem. Rev.* **121**(5), 2857–2897 (2021).
3. B. Göbel, I. Mertig, and O. A. Tretiakov, "Beyond skyrmions: review and perspectives of alternative magnetic quasiparticles," *Phys. Rep.* **895**, 1–28 (2021).
4. S. Tsesses et al., "Optical skyrmion lattice in evanescent electromagnetic fields," *Science* **361**(6406), 993–996 (2018).
5. A. Karnieli et al., "Emulating spin transport with nonlinear optics, from high-order skyrmions to the topological Hall effect," *Nat. Commun.* **12**(1), 1092 (2021).
6. L. Du et al., "Deep-subwavelength features of photonic skyrmions in a confined electromagnetic field with orbital angular momentum," *Nat. Phys.* **15**(7), 650–654 (2019).
7. T. J. Davis et al., "Ultrafast vector imaging of plasmonic skyrmion dynamics with deep subwavelength resolution," *Science* **368**(6489), eaba6415 (2020).
8. Y. Shen et al., "Supertoroidal light pulses as electromagnetic skyrmions propagating in free space," *Nat. Commun.* **12**(1), 5891 (2021).
9. S. Gao et al., "Paraxial skyrmionic beams," *Phys. Rev. A* **102**(5), 053513 (2020).
10. Y. J. Shen, E. C. Martínez, and C. Rosales-Guzmán, "Generation of optical skyrmions with tunable topological textures," *ACS Photonics* **9**(1), 296–303 (2022).
11. W. Lin et al., "Microcavity-based generation of full Poincaré beams with arbitrary skyrmion numbers," *Phys. Rev. Res.* **3**(2), 023055 (2021).
12. Y. Shen et al., "Topological transformation and free-space transport of photonic hopfions," *Adv. Photonics* **5**(1), 015001 (2023).
13. R. Gutiérrez-Cuevas and E. Pisanty, "Optical polarization skyrmionic fields in free space," *J. Opt.* **23**(2), 024004 (2021).
14. P. B. Corkum, "Plasma perspective on strong field multiphoton ionization," *Phys. Rev. Lett.* **71**(13), 1994 (1993).
15. T. Popmintchev et al., "Bright coherent ultrahigh harmonics in the keV x-ray regime from mid-infrared femtosecond lasers," *Science* **336**(6086), 1287–1291 (2012).
16. J. Wätzel and J. Berakdar, "Topological light fields for highly nonlinear charge quantum dynamics and high harmonic generation," *Opt. Express* **28**(13), 19469–19481 (2020).
17. M. Zurch et al., "Strong-field physics with singular light beams," *Nat. Phys.* **8**(10), 743–746 (2012).
18. K. M. Dorney et al., "Controlling the polarization and vortex charge of attosecond high-harmonic beams via simultaneous spin–orbit momentum conservation," *Nat. Photonics* **13**(2), 123–130 (2019).
19. L. Rego et al., "Generation of extreme-ultraviolet beams with time-varying orbital angular momentum," *Science* **364**(6447), eaaw9486 (2019).
20. F. Kong et al., "Controlling the orbital angular momentum of high harmonic vortices," *Nat. Commun.* **8**(1), 14970 (2017).
21. D. Gauthier et al., "Tunable orbital angular momentum in high-harmonic generation," *Nat. Commun.* **8**(1), 14971 (2017).
22. L. Rego et al., "Nonperturbative twist in the generation of extreme-ultraviolet vortex beams," *Phys. Rev. Lett.* **117**(16), 163202 (2016).
23. Y. Fang, S. Lu, and Y. Liu, "Controlling photon transverse orbital angular momentum in high harmonic generation," *Phys. Rev. Lett.* **127**(27), 273901 (2021).

24. A. Yang et al., "Spin-manipulated photonic skyrmion-pair for picometric displacement sensing," *Adv. Sci.* **10**(12), 2205249 (2023).
25. K. S. Youngworth and T. G. Brown, "Focusing of high numerical aperture cylindrical-vector beams," *Opt. Express* **7**(2), 77–87 (2000).
26. K. Y. Bliokh, A. Y. Bekshaev, and F. Nori, "Dual electromagnetism: helicity, spin, momentum and angular momentum," *New J. Phys.* **15**(3), 033026 (2013).
27. K. Y. Bliokh, J. Dressel, and F. Nori, "Conservation of the spin and orbital angular momenta in electromagnetism," *New J. Phys.* **16**(9), 093037 (2014).
28. Y. Fang et al., "Photoelectronic mapping of the spin–orbit interaction of intense light fields," *Nat. Photonics* **15**(2), 115–120 (2021).
29. Y. Fang et al., "Strong-field photoionization of intense laser fields by controlling optical singularities," *Sci. China Phys. Mech. Astron.* **64**(7), 274211 (2021).
30. A. Fleischer et al., "Spin angular momentum and tunable polarization in high-harmonic generation," *Nat. Photonics* **8**(7), 543–549 (2014).
31. D. A. Kessler and I. Freund, "Lissajous singularities," *Opt. Lett.* **28**(2), 111–113 (2003).
32. W. Miao and G. Gbur, "Design of Lissajous beams," *Opt. Lett.* **47**(2), 297–300 (2022).
33. M. Lewenstein et al., "Theory of high-harmonic generation by low-frequency laser fields," *Phys. Rev. A* **49**(3), 2117 (1994).
34. N. Nagaosa and Y. Tokura, "Topological properties and dynamics of magnetic skyrmions," *Nat. Nanotechnol.* **8**(12), 899–911 (2013).
35. X. Yi et al., "Hybrid-order Poincaré sphere," *Phys. Rev. A* **91**(2), 023801 (2015).
36. Y. Shen et al., "Roadmap on spatiotemporal light fields," arXiv:2210.11273 (2022).
37. Y. Fang et al., "Probing the orbital angular momentum of intense vortex pulses with strong-field ionization," *Light Sci. Appl.* **11**(1), 34 (2022).
38. K. Litzius et al., "Skyrmion Hall effect revealed by direct time-resolved X-ray microscopy," *Nat. Phys.* **13**(2), 170–175 (2017).
39. J. Miao et al., "Beyond crystallography: diffractive imaging using coherent x-ray light sources," *Science* **348**(6234), 530–535 (2015).

Biographies of the authors are not available.